Chapter 3

Electro-oxidation of formic acid for the production of hydrogen on polycarbazole-WO_3 composite-modified electrodes

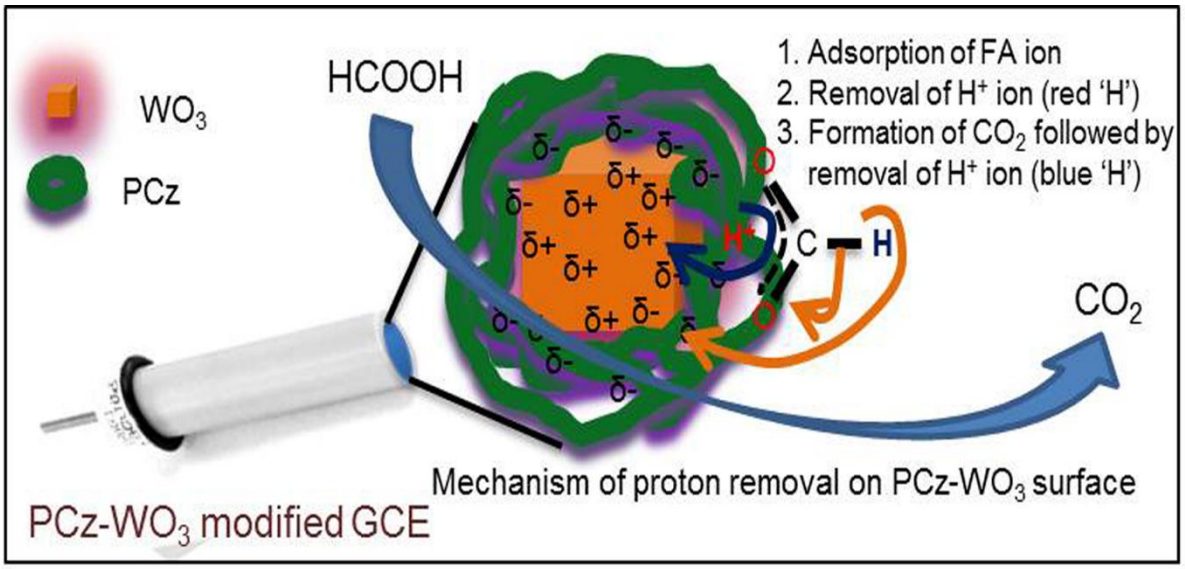

This chapter discusses the electro-oxidation of formic acid properties of polycarbazole/WO_3 composites (PCz/WO_3) prepared using various weight % of WO_3 incorporated into the fixed PCz matrix at the monomeric level. This investigation sheds light on exploring low-cost, environmentally friendly electrocatalysts with performance as an alternative for noble metal.

3.1. Introduction

Formic acid (FA) as a fuel in fuel cell applications has attracted considerable interest because of mainly two reasons: First, it makes better and easy proton transport on the catalyst with thermodynamic potential and second, eco-friendly, recyclable, less hazardous, and non-inflammable compared to methanol or even ethanol in the diluted form [38], [76], [77]. The mechanism of FA oxidation follows triple pathways, starting with FA adsorption followed by the adsorbents that can either directly oxidize it to CO_2 (direct pathways) [78], [79] secondly bridged-adsorbed dehydrogenation as formate (formate pathways) or undergoes carbon monoxide adsorbed dehydration (indirect pathways which are due to non-faradaic dissociation of FA) [79], [80]. The direct paths are more suitable as FA quickly oxidizes to CO_2 without forming a toxic CO intermediate. There are various reports available on the oxidation of FA using different catalysts like noble metal and their combinations Pt, Pd, Au [81], [82], [83], Pt-Ru and Pt-Au [84], Pt-Pd [85], [86], bimetals with non-noble metals Pd-Co [87], Pd-Cu [88], Pt-Ir [89], Pt-Ni [90], Pd-Ag [91], Fe-Pt [92], Pt-Zn [93], metal oxides TiO_2 [94], PbO [95], CeO_2 [96], [97], Pd-CeO_2 [98], IrO_2 [99], Pt-MnOx [100], [101], TiOx/Pt [102], Pt-Pd/WO_3-OMC [103] and conductive polymers like PANI [104], [51], PIN [105], [106], [107], [53], PTh [108], [109], PPy [110], [111], [112], [113], and PCz [114], [115], [54]. However, Pt metal catalyst shows dual pathways mechanism (direct and indirect pathways) for FA oxidations. To overcome this problem, Pt-based composites came into existence as a catalyst. However, their preparations are very lavish because of the complex synthesis and the high cost of the noble metals. Furthermore, other metals like Pd, Au, and transition metals are considered well-suited catalysts for the oxidation of FA to CO_2. Nevertheless, corrosion of these metals in a given environment (like acidic/basic electrolyte media or CO intermediate poisoning) again restricted their use as electrode material. Metal oxides and metal oxide-based composites are expected to

be an improved alternative to conquer these limitations. It is also examined that mainly the filler components of composite-based catalyst at the working/anode electrode control the complete efficiency of the cell assembly [107], [54]. These materials are crucial for fuel cells' steady and efficient performance since they may influence charge conductivity, catalyst diffusion, and stability. Consequently, it is necessary to develop an economically and environmentally favorable route. In metal oxides, especially WO_3 is an important reducible transition metal oxide with a high oxygen-carrying capacity [116], [117], [118]. It also has the capability to enhance the adsorbed CO intermediate removal from the electrode surfaces due to its oxophilic nature [119]. The nanostructured WO_3 is a potential material for many applications, like photocatalysts, catalysts, gas sensors, solar energy, field emission and electrochromic devices [118]. At the same time, the monoclinic structure of WO_3 is much more stable relative to other WO_3 structures because it consists of a 3D network of WO_6 octahedrons [120]. The transition metals allow themselves to switch in-between valence states due to partially filled d- and f-orbitals. Different methods for synthesizing WO_3 nanostructures, such as chemical vapor deposition, sol-gel methods, hydrothermal methods, magnetron sputtering, chemical precipitations, and electrochemical depositions, are already approached. These methods yield different morphologies like spherical nanoparticles, flake-wall-like, nano-plate-like, nano-sheet-like, nanowires, nanorods, nano-porous, nano bowl structures morphology, etc. [120], [121]. Amongst them, the nano-plate morphology shows excellent catalytic properties due to surface site density. However, nano-architectural assemblies have the ability to agglomerate together due to their high surface energy. So, stabilizing these nanoparticles by CP additive is one of the efficient approaches. CPs are regarded as excellent candidates due to their broad potential applications in catalysis, sensor, charge storage, and micro/nanoelectronics [122], [123], [124], [125], [126]. Heterocyclic PCz is one of the CPs that can easily share electrons

with electron-deficient moieties. At the same time, environmental stability and good conducting properties make it a potential candidate for different applications from sensors to electronics to catalysis [125], [126], [127].

In the present work, we have synthesized three different PCz-WO_3 nanocomposites by varying the amount of nano WO_3 and polymerizing a fixed amount of carbazole monomer at the interface of two immiscible liquids with the help of ammonium persulphate (APS) oxidant. As-synthesized PCz-WO_3 nanocomposites were characterized by UV-Visible, XRD, FTIR, SEM, and TEM for their optical, structural and morphological illustrations. After modifying the glassy carbon electrodes (GCE) with these nanocomposite catalysts, the electrocatalytic properties were investigated by DPV, EIS and chronoamperometry (CA) potentiodynamic method in a highly acidic medium (0.5M H_2SO_4 + 1M HCOOH electrolyte).

3.2. Experimental section

3.2.1 Materials

Sodium tungstate dihydrate extra pure AR (99 %) was purchased from SRL, India. Formic acid, Conc. HCl (37 %), dichloromethane (AR grade), and ammonium persulphate (extra pure AR grade, (99 %) were obtained from Merck, India. Carbazole crystalline (>95 %) was procured from Sigma-Aldrich. All the chemicals were used as received.

3.2.2 Synthesis of nano WO_3

Nano WO_3 is synthesized successfully by the coprecipitation technique [120], [121]. Firstly, 100.0 mL of 15.0 mM sodium tungstate solution was prepared in deionized water. To this solution, 45.0 mL of 6.0 M HCl was added drop by drop at room temperature under constant stirring at 500 rpm till the pH of the solution became 2.0. The reaction mixture was stirred further for about 8 h to get a pale-yellow color precipitate due to the formation of tungstic acid.

$$Na_2WO_4 + 2HCI \rightarrow H_2WO_4 + 2NaCI \qquad \text{(eq. 3.1)}$$

where H_2WO_4 is the tungstic acid.

After filtering the precipitate, dilute HCl solution was used to wash several times, followed by DI water till the pH of the filtrate became 7.0. After that, this precipitate was dried in a vacuum oven at 60 °C for 24 h followed by calcination at 700 °C for 6 h.

3.2.3 Synthesis of PCz and PCz-WO_3 nanocomposites

Initially, PCz was synthesized using an interfacial method [79]. Herein, 84.0 mg (25 mM) carbazole (Cz) monomer was dissolved in 20.0 mL dichloromethane in a stoppered conical flask (say solution A). Next, 228 mg (50 mM) APS was dissolved in 20.0 mL of DI water (say solution B). Now, B solution was added slowly to A through the wall of the conical flask. Polymerization is carried out at the interface of the aqueous and non-aqueous mediums. For complete polymerization, the above reaction mixture was kept for 24 h, washed with dichloromethane (to remove unreacted monomers) and water (to remove unreacted APS), and kept for drying at 60 °C in a vacuum oven.

To synthesize PCz-WO_3 nanocomposites, 84.0 mg nano WO_3 (properly ground) powder was added to solution A (25 mM) and stirred at 700 rpm for one hour. After that, polymerization was started similarly using solution B (50 mM), as mentioned above. This as-synthesized nanocomposite is designated as PCz-WO_3/1 in the whole manuscript. Similarly, two other nanocomposites were also synthesized by taking 42.0 mg and 21.0 mg nano WO_3 using similar synthesis conditions and designated as PCz-WO_3/2 and PCz-WO_3/4, respectively.

3.2.4 Electrode modification

First, GCE was cleaned using a slurry of 0.4 μM alumina on a polishing cloth. After that, the polished surface of GCE was modified by 10.0 μL of various PCz-WO_3 nanocomposites dispersion prepared in tetrahydrofuran (THF) solvent. The dispersion was prepared by adding

2.0 mg of PCz-WO_3 nanocomposites in 1.0 mL THF and using ultrasonication for 30 min. For comparison purposes, GCE was also modified by 10.0 μL dispersions of PCz and WO_3 independently.

3.3. Results and discussion

It is interpreted that the surface charge of the metal oxides cluster can be controlled based on pH, which makes it a potential candidate for interacting with nearby environments [128]. For example, if we consider the case of WO_3, it has a point of zero charges (PZC) at pH=1.9-2.5 [128]. It means the surface charge of WO_3 is neutral at this pH. The surface charges become positive below PZC due to WO_2OH^+ (aq.) formation and become negative above PZC due to the formation of WO_4^{2-} [128]. On the other hand, multiple conjugated bonds and heterocyclic moieties in PCz polymer enhance the availability of electron centers that can share their electrons with electron-deficient centers. At the same time, it has positive charge centers on its backbone (due to doping during polymerization) that can easily interact with electron-rich centers [79]. These facts might be a concrete reason for the adsorption of formate ions and the electro-oxidation of FA by the dehydrogenation-dominated process (direct process), as discussed later in the electrocatalytic activity section. Prior to this, as-synthesized materials are characterized for their existence (non-disturbance of their identity even after *in-situ* polymerization conditions) by various tools described below.

3.3.1 Structural characterizations

To study the optical properties of PCz, WO_3, PCz-WO_3/1, PCz-WO_3/2, and PCz-WO_3/4 UV-Visible characterization was done initially (shown in Fig.1). PCz exhibits peaks at 234 nm corresponding to $\pi \rightarrow \pi^*$ transition, 257 nm due to polaron$\rightarrow\pi^*$ transition in the conduction band, which is the consequence of extended conformation within the polymeric chain and 293 nm corresponds to bipolaronic transition. (Fig. 3.1(I)) [79]. WO_3 exhibits three absorption peaks

at 207, 256, and 359 nm corresponding to the tungsten trioxide, poly tungstate species, and charge transfer to W^{6+} species, respectively (Fig. 3.1(I)) [129], [130]. The absorption peaks of PCz are dominated in all the cases of PCz-WO_3 composites from 234 to 293 nm. Apart from this, the PCz-WO_3 composite has another absorption peak at 335 nm, which corresponds to the interaction between PCz and WO_3 (Fig. 3.1 (I)). The peak that came at 359 nm in WO_3 has shifted to 335 nm due to electron transfer from the electron-rich centers of PCz to electron-deficient centers of WO_3. The absorption peak at 335 nm goes on decreasing in the case of PCz-WO_3/2 and PCz-WO_3/4 due to the decrease in WO_3 content. The variation in the dominancy of WO_3 can be visualized in fig. 3.1(II).

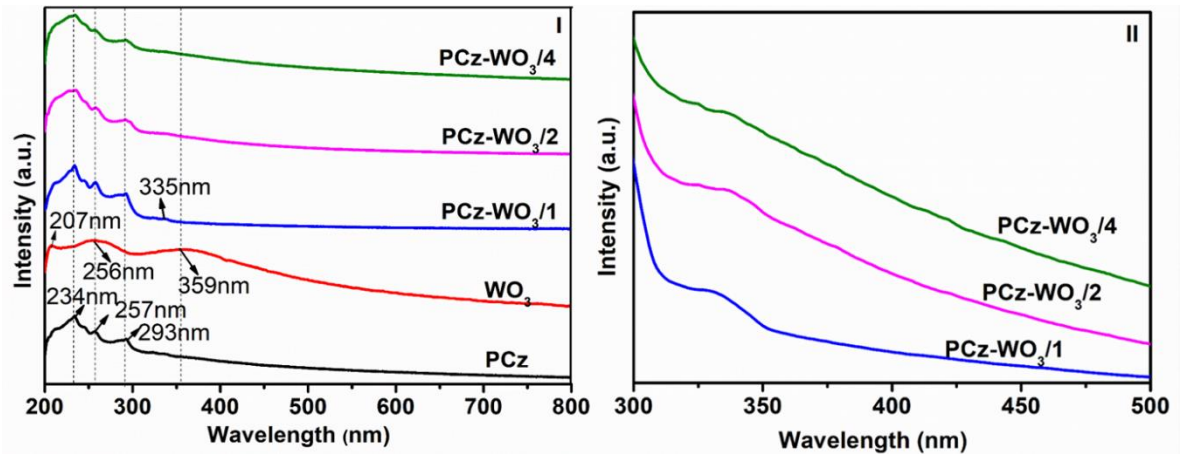

Figure 3.1: (I) UV-Visible absorption spectra (in 1 cm cuvette length) of PCz, WO_3, PCz-WO_3/1, PCz-WO_3/2 and PCz-WO_3/4 and (II) enlarged view of fig 3.1(I) from 300 to 500 nm.

XRD was performed to determine the existence of pure phase in as-synthesized WO_3 nanoparticles as well as in WO_3-PCz composite. PCz exhibits two broad diffraction peaks around $2\theta=22^o$ and 43.08^o, along with some sharp peaks over the broad peak background. The broad diffraction peak arises due to its amorphous nature, while sharp peaks correspond to the crystalline zones in the PCz lattice (Fig. 3.2(I)) [79]. As shown in the spectra (fig. 3.2(II)), the

entire diffraction peaks of WO_3 match very well with the monoclinic phase (JCPDS No. 01-083-0950) belonging to the Hermann-Mauguin space group 'P 1 21/n 1' and space group no. 14. To assure the monoclinic structure of the WO_3 nanocrystals, XRD profile matching & integrated intensity refinement are performed using FullProf.2k (Version 5.40 - Mar2014-ILL JRC). Since the XRD pattern is well matched with the simulated one, various parameters are calculated using the Le Bail fitting and summarized in Table 3.1. The profile fitting confirms that the as-prepared WO_3 revealed no additional peaks other than the monoclinic phase and reaffirms its high purity. In the case of WO_3-PCz composites, an explicit amorphous nature is observed to be increased in the spectra with increasing polymer contents. Due to the high scattering factor of crystalline WO_3, diffraction peaks appear over the amorphous background of polymers. Herein, WO_3 exhibits all characteristic peaks even in its composite form, which exemplifies the retention of its identity. It is again rechecked by fitting the XRD pattern of PCz-WO_3/4 (high content of PCz) and keeping all similar fitting parameters (Fig. 3.2(III)). Comparing the refinement parameters of the XRD pattern corresponding to PCz-WO_3/4 and WO_3, the unit cell dimension remains constant. It maintains its phase purity despite loading a high amount of PCz polymer (Table 3.1).

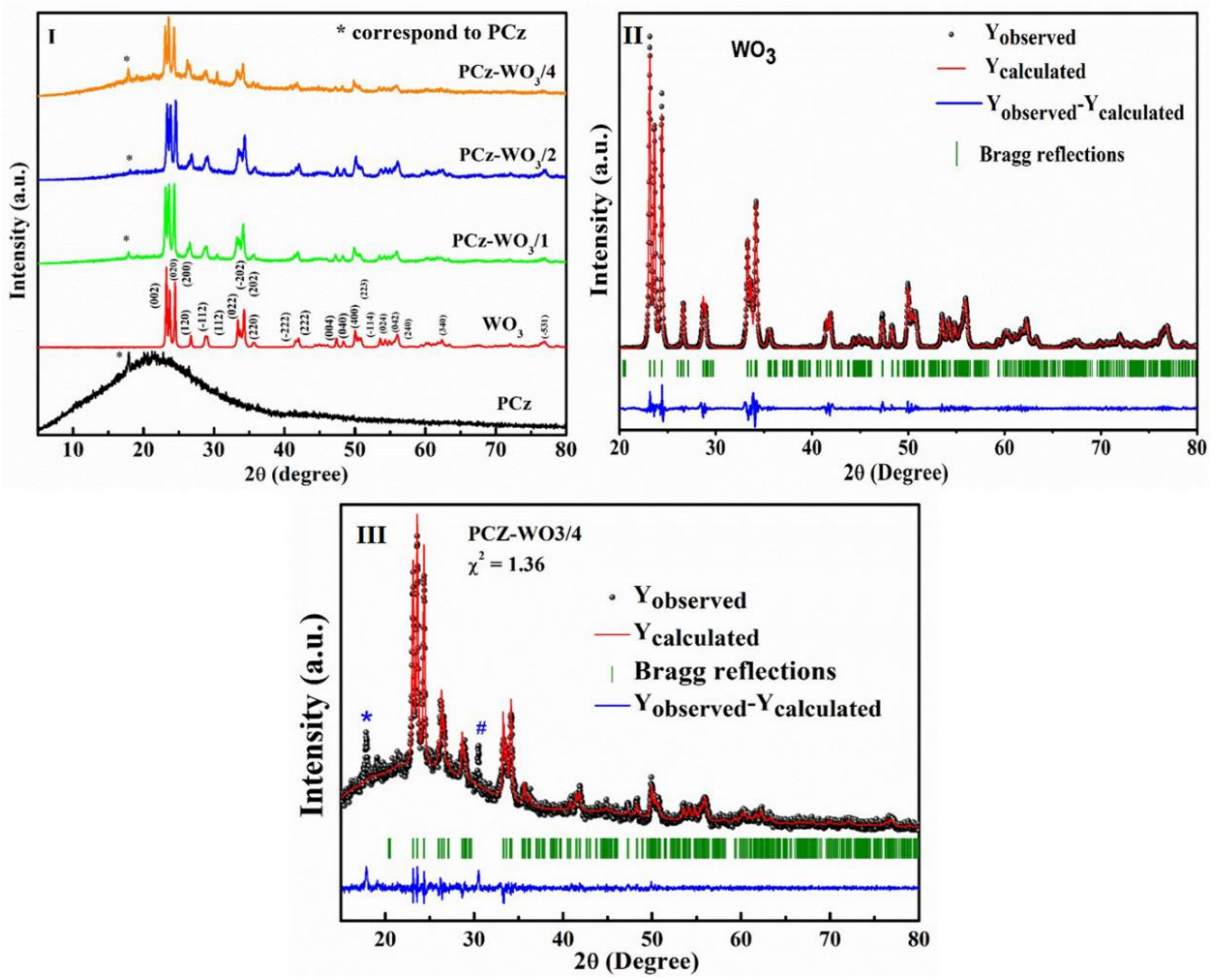

Figure 3.2: (I) X-ray diffraction pattern of PCz, WO_3, PCz-WO_3/1, PCz-WO_3/2 and PCz-WO_3/4, Le Bail profile matching and integrated intensity refinement of (II) WO_3 and (III) PCz-WO_3/4.

Table 3.1: Structural parameters for WO_3 and PCz-WO_3/4 from Le-ball profile fitting.

Structural parameters	**a (Å); b (Å); c (Å)**	**Volume (Å^3)**	**α (°); β (°); γ (°)**	**R_p; R_{wp}**	**χ^2**
WO_3	7.30; 7.53; 7.69	422.60	90.0; 90.71; 90.0	7.37; 11.3	3.16
PCz-WO_3/4	7.31; 7.54; 7.69	422.42	90.0; 90.70; 90.0	7.01; 9.12	1.48

The chemical functionalities of PCz, WO_3, and all composites were correlated by FTIR spectroscopy in ATR mode (Fig. 3.3). PCz exhibits vibration peaks at 725.10 cm^{-1} due to ring deformation of a substituted aromatic ring. The peak at 806.60 cm^{-1} and 875.85 cm^{-1} are due to tri-substituted benzene, confirming para-substitution and polymerization took place at 3 and 6 positions [79]. CH_2 rocking vibration owing to tail-to-tail addition consequence peaks around 746.10 cm^{-1}. The 1050 cm^{-1} peaks correspond to dopant ions, and 1229.94 cm^{-1} is associated with C=N stretching [79]. Peaks around 1324.44 cm^{-1} correspond to the bending vibration of C-H out-of-plane in the aromatic ring, and 1450.61 cm^{-1} is related to the ring stretching vibration of Cz moiety [79]. The vibration peak at 1490.22 cm^{-1} is due to C-N stretching. The vibration 1620 cm^{-1} corresponds to the C-N stretching of the C-N bond of a disubstituted benzene ring and 3058.17 cm^{-1} and 3403.74 cm^{-1} correspond to N-H stretching in the PCz unit, respectively [79]. WO_3 exhibits the vibration peak at 588.34 cm^{-1} related to the stretching mode of the O-W bond. The vibration peaks of about 915.45 cm^{-1} related to the v(O-O) and v(W-O-W) stretching of bridging oxygen of the WO_6 octahedron sharing corner in the WO_3 crystal [131]. The peak at 1003.73 cm^{-1} corresponds to W=O stretching (short) mode [131] and the peak of about 1596.04 cm^{-1} is due to the adsorbed water O-H bending vibration on the WO_3. In addition to this, the peak at 3372.41 cm^{-1} corresponds to the O-H stretching mode of coordinated water molecules [131]. In the case of all PCz-WO_3 nanocomposites, the characteristic peaks associated with the individual components are present, which signifies its existence even in the composite state. However, peak dominancy depends on the amount of individual content. For example, the vibration peak of PCz-WO_3/1 (high content of WO_3) present at 915, 1003 and 3372 cm^{-1} are almost going to vanish compared to PCz-WO_3/4 (high content of PCz).

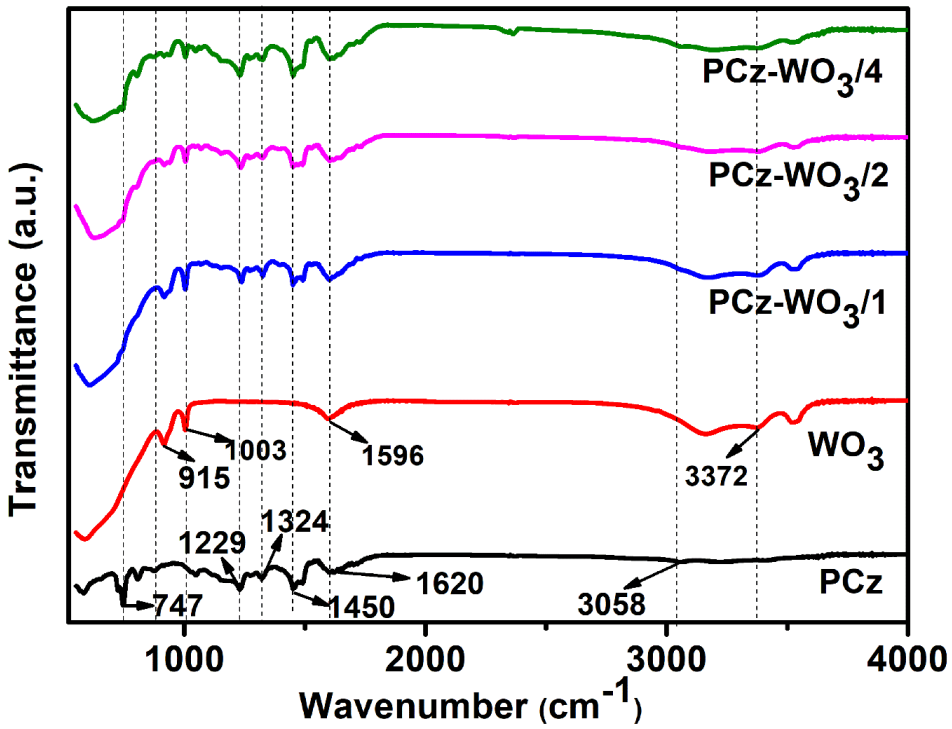

Figure 3.3: FTIR spectrum of PCz, WO_3, PCz-WO_3/1, PCz-WO_3/2 and PCz-WO_3/4.

3.3.2 Morphological characterization

Morphological textures of PCz, WO_3, PCz-WO_3/1, PCz-WO_3/2 and PCz-WO_3/4 were analyzed by SEM and TEM (Fig. 3.4 and Fig. 3.5). PCz exists in the form of large flake thickness lies in the 730-780 nm range and flake size lies in some micron range. These flakes are oriented randomly in a wrinkled state. PCZ is amorphous, as evident from its SAED pattern and consistent with the XRD (Fig. 3.4a, 3.5a and 3.5a'). WO_3 is highly crystalline (as evidenced in SAED and XRD patterns) and has cube-like morphology which is fused in the nanometric range. This improper fusion elongated its shapes in an inhomogeneous fashion (Fig. 3.4b, 3.5b and 3.5b'). These particles are embedded inhomogeneously over the PCz flakes in the case of PCz-WO_3/1 and PCz-WO_3/2 nanocomposites (*see* the circled area of Fig. 3.4c and 3.4d). But, PCZ dominates in the case of PCz-WO_3/4, which is why WO_3 cannot be seen here. However,

a clear existence of the nano WO_3 in either case of its nanocomposite form can be seen in the transmission mode of TEM (*see* Fig. 3.5c, 3.5d and 3.5e). As soon as polymer content increases, the extent of amorphous behavioral increases, as evidenced in the SAED pattern of PCz-WO_3/1, PCz-WO_3/2 and PCz-WO_3/4.

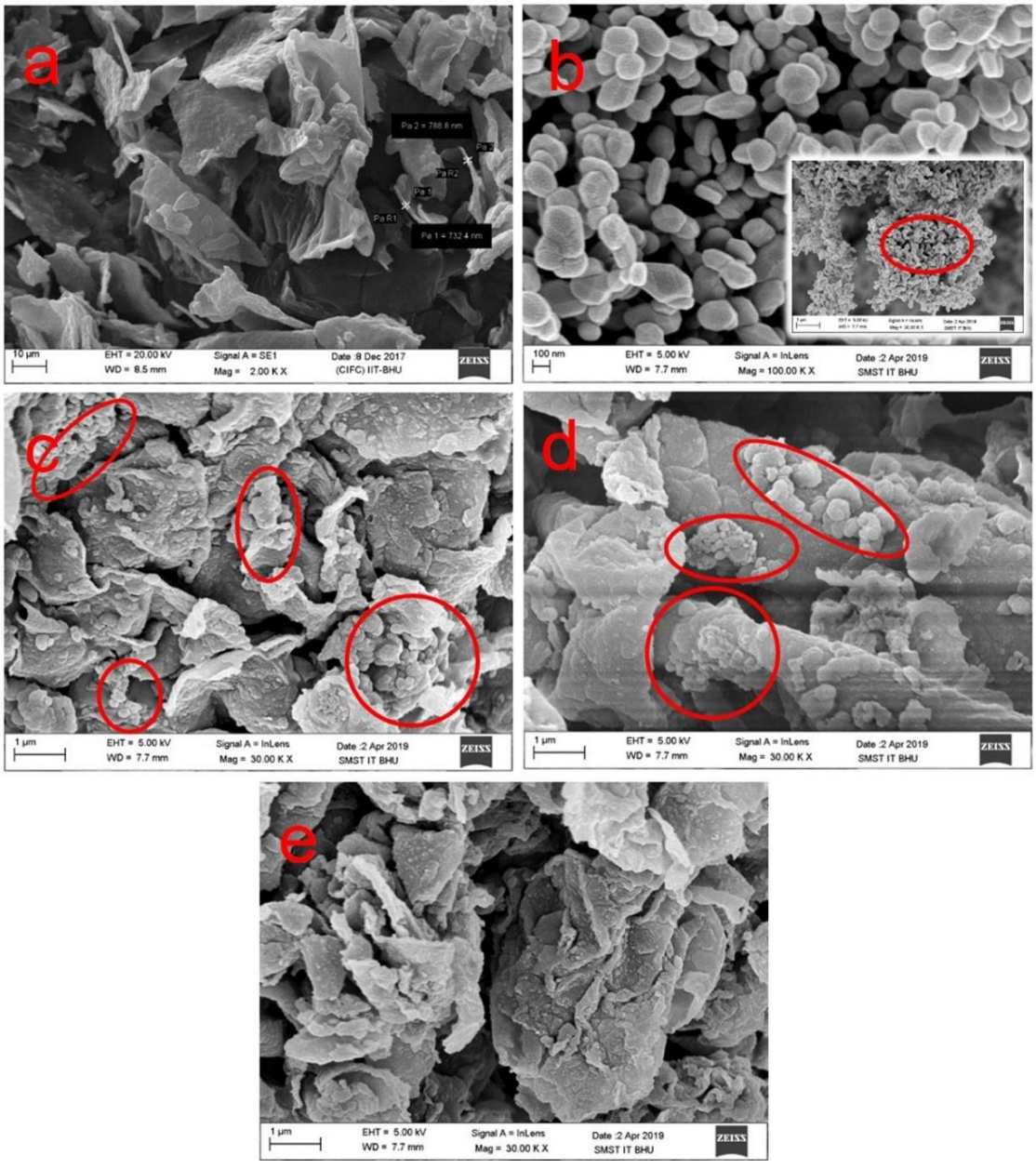

Figure 3.4: SEM of (a) PCz, (b) WO_3, (c) PCz-WO_3/1, (d) PCz-WO_3/2 and (e) PCz-WO_3/4. Encircled area of the inset of fig. 4b shows zoomed view of WO_3 as attached in 4b.

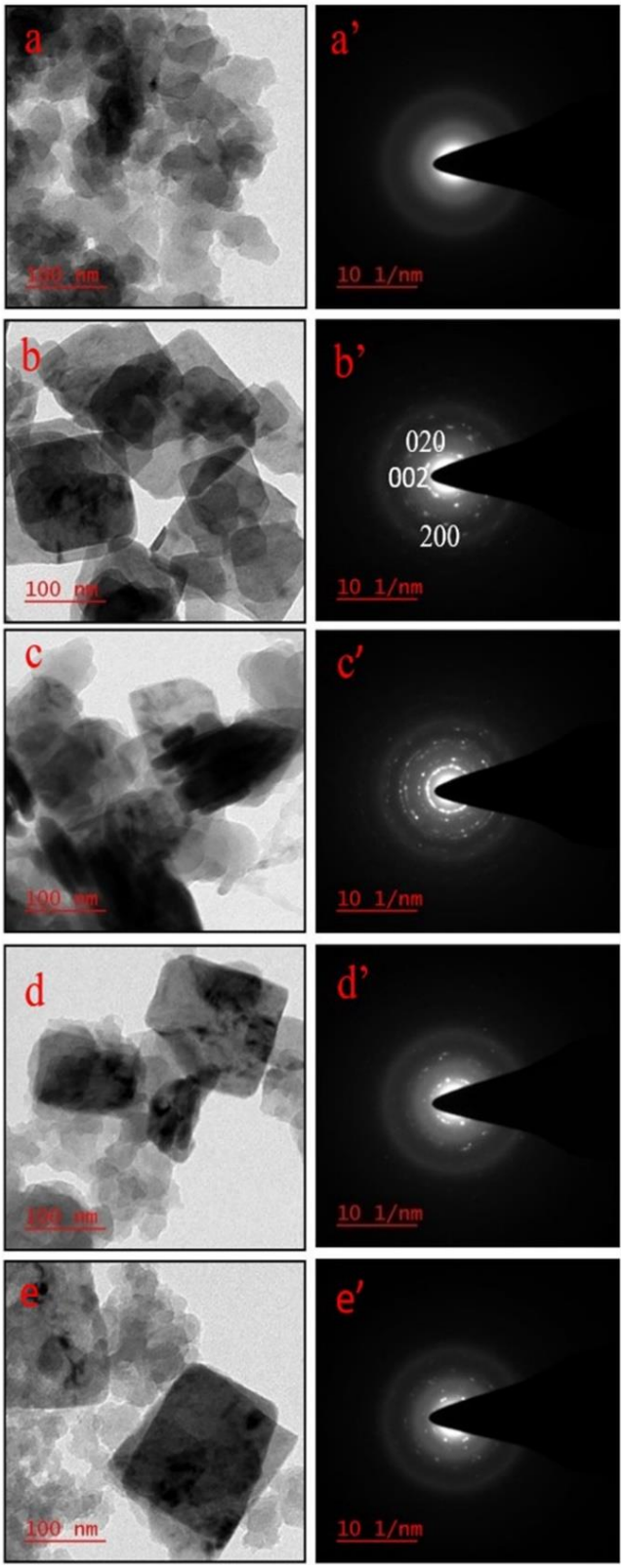

Figure 3.5: TEM image and SAED pattern of (a, a') PCz, (b, b') WO_3, (c, c') PCz-WO_3/1, (d, d') PCz-WO_3/2 and (e, e') PCz-WO_3/4.

3.3.3. Electrocatalytic activity

The electrocatalytic activity of PCz-WO_3/1, PCz-WO_3/2 and PCz-WO_3/4 nanocomposites were investigated and compared with as-synthesized PCz and nano WO_3 towards electro-oxidation of FA after the modification of commercial GCE by these materials. First, electro-oxidation was performed by DPV technique and the observed I-V response is shown in Fig.3.6. Prior to the FA oxidation activity, all the above electrodes are checked for its response in supporting electrolyte (0.5 M H_2SO_4) only (as shown in figure 3.6 (I)). This figure shows that there is no well-resolved peak in the given potential window. It means that modified electrodes are not contributing to any electrode reaction. After that, a mixture of 0.5 M H_2SO_4 and 1.0 M HCOOH was used for the electrode activity test and the resulting responses are shown in figure 3.6 (II). In general interpretation, the electro-oxidation of FA proceeds with two well-resolved oxidation potentials curvature at 0.36 to 0.49 V and 0.58 to 0.70 V using modified commercial GCE [106], [53]. The lower range potential corresponds to direct oxidation, while the higher potential end corresponds to indirect oxidation (involvement of poisonous CO) [132]. From Fig. 3.6, it is exemplified that PCz exhibits oxidation corresponding to direct oxidation at 0.36 V while nano WO_3 supports oxidation via the involvement of both direct and indirect pathways at 0.25 V and 0.41 V, respectively (Fig. 3.6). PCz-WO_3/1, PCz-WO_3/2 and PCz-WO_3/4 nanocomposites modified commercial GCEs exhibit electro-oxidation response at 0.26 V and 0.42 V corresponding to the involvement of direct and indirect pathways respectively. However, on comparing these electro-oxidation responses, the oxidation curvature of PCz-WO_3/4 observed at 0.42 V going to suppress compared to that of PCz-WO_3/1 or PCz-WO_3/2 (Fig. 3.6). This is due to higher PCz content, effective for increasing charge density at the vicinity of nano WO_3 surface similar to the effect between metals or metal oxides and polymer or macrocyclic compounds and results in CO tolerance during oxidation of FA [53], [133].

These results are consistent with the oxidation at potentiostatic conditions by CA, as discussed later.

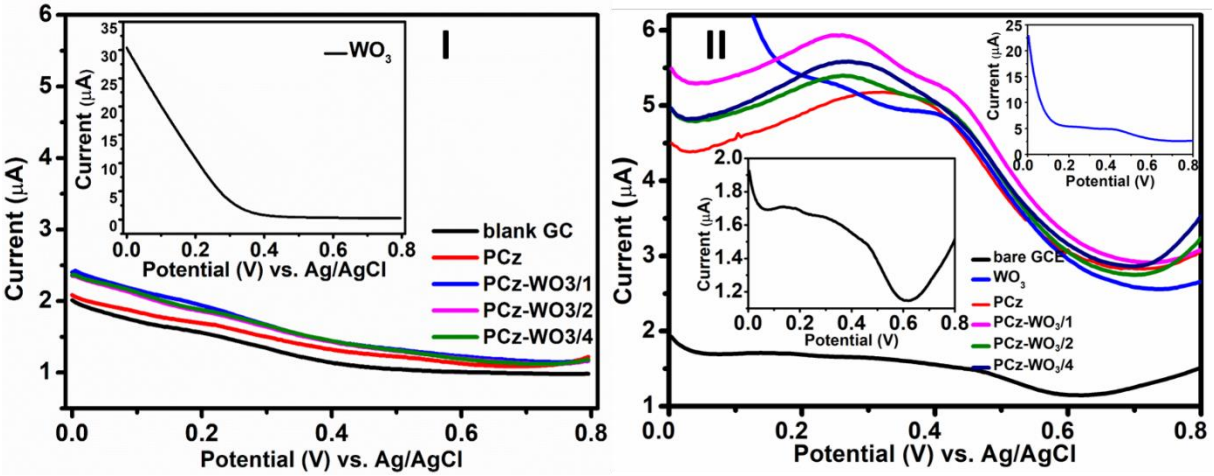

Figure 3.6: DPV (anodic scan) of PCz, WO_3, PCz-WO_3/1, PCz-WO_3/2 and PCz-WO_3/4 *vs.* Ag/AgCl in (I) 0.5 M H_2SO_4 only and (II) 0.5 M H_2SO_4 + 1.0 M HCOOH. In figure 3.6 (II), the lower inset indicates the DPV response of bare GCE and the upper inset indicates the DPV response of WO_3.

The electro-oxidation activity and stability of PCz, WO_3, PCz-WO_3/1, PCz-WO_3/2 and PCz-WO_3/4 nanocomposites were analyzed and compared by the CA method at potentials 0.26 V (associated with direct oxidation) and 0.42 V (associated with indirect oxidation) *vs.* Ag/AgCl for the periods of 500 s in 0.5 M H_2SO_4 containing 1.0 M HCOOH as shown in Fig.3.7. It is already interpreted that, the saturation in current density concerning the passage of time is a direct consequence of good electrode activity and stability [134]. On comparing all composites, PCz-WO_3/4 exhibits the highest saturation current density at 500 s indicating better electrode activity towards direct oxidation of formic acid compared to that of other compositions. This is due to the high content of PCz that enhances the optimal amount of charge at the nano WO_3 surface (Fig. 3.7I and table 3.2). Almost the same trends were observed in the variation of current densities when oxidation is carried out at 0.42 V (Fig 3.7II and table 3.2).

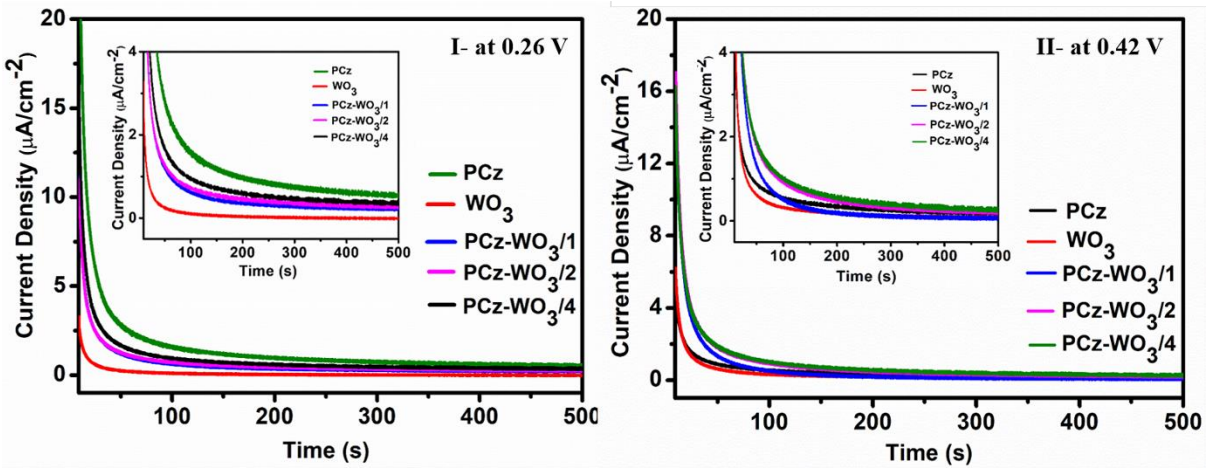

Figure 3.7: CA of PCz, WO_3, PCz-WO_3/1, PCz-WO_3/2 and PCz-WO_3/4 at (I) 0.26 V and (II) 0.42 V *vs*. Ag/AgCl in 0.5 M H_2SO_4 containing 1.0 M HCOOH. Inset shows zoomed view of similar and respective plots.

Table 3.2: Current densities of different electrodes in potentiostatic condition at 500 s *vs.* Ag/AgCl.

Materials	**Current Density (in μAcm^{-2})**	
	At 0.26 V	**At 0.42 V**
PCz	0.54	0.17
WO_3	0.02	0.08
PCz-WO_3/1	0.21	0.06
PCz-WO_3/2	0.27	0.19
PCz-WO_3/4	0.36	0.25

After the stability test, the electrochemical impedance behavior of PCz, WO_3, PCz-WO_3/1, PCz-WO_3/2 and PCz-WO_3/4 were analyzed by EIS at open circuit potentials (OCP), 0.26 V and 0.42 V from 10 kHz to 10 mHz frequencies range and as-observed curves are represented as Nyquist plots in Fig. 3.8. Based on this plot, various types of applications like catalysis, sensor and biosensor, charge storage, photo-electrocatalysis, etc. can be interpreted utilizing the charge

transfer phenomenon [106], [119], [121]. Usually, the Nyquist curve's inclination toward the Z''-axis indicates a higher charge deposit near the electrode surface [135]. The electrode's diffusion-dominated mass transfer behavior results in the development of a straight line, whereas resistance to charge transfer results in forming a semicircle inclined towards the Z'-axis [136]. On this basis, at OCP, PCz is more resistive among others and nano WO_3 has a high capability to store charge over its surface (Fig. 3.8I). However, at a high-frequency range (near the origin), PCz and all nanocomposites have relatively higher resistance to charge transfer properties than nano WO_3 due to the semiconducting nature of PCz. That is why these materials are exhibiting almost similar behavior in this range (*see* inset of Fig. 3.8I). As soon as time passes (or towards lower frequencies range), the contribution of nano WO_3 shows a decisive role towards electro-activity and vertically shifted towards Z''-axis concerning PCz due to charge accumulation near the electrode surface (*cf.* Fig. 3.8I). Due to the high content of PCz in PCz-WO_3/4 results, diffusion dominated charge transfer at the electrode surface and hence showed more sluggish charge transfer behavior than that of PCz-WO_3/1 and PCz-WO_3/2 at either case of applied potentials (*cf.* EIS nature of PCz-WO_3/1, PCz-WO_3/2 and PCz-WO_3/4 of Fig. 3.8I, 3.8II and 3.8III). On comparing the behavior of PCz-WO_3/4 at OCP, 0.26 and 0.42 V, PCz-WO_3/4 exhibit low resistance to charge transfer at higher frequencies ranges with more charge accumulation near the electrode surface as time passes (at lower frequencies range) on OCP (*cf.* Fig. 3.8IV with inset of Fig. 3.8IV). However, it has almost the same behavior at 0.26 and 0.42 V in the initial period of experimentations (at a higher frequency range). But as soon as time passes, the EIS curve obtained at 0.42 V exhibit more inclination towards the Z''-axis than that of the EIS curve obtained at 0.26 V due to more charge accumulation near the electrode surface by adherence of both CO and CO_2 moieties during the oxidation of FA (*cf.* Fig. 3.8IV).

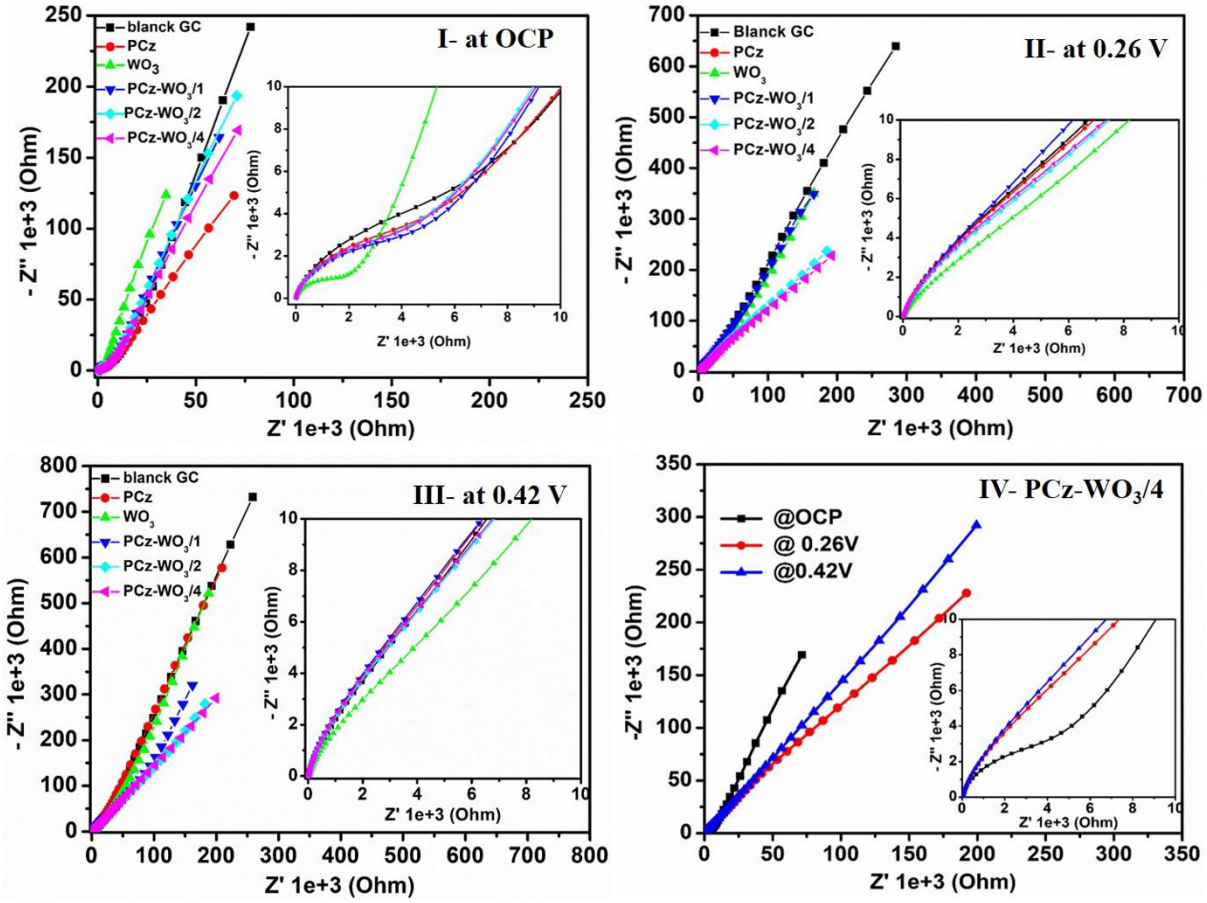

Figure 3.8: EIS of PCz, WO_3, PCz-WO_3/1, PCz-WO_3/2 and PCz-WO_3/4 at (I) OCP, (II) 0.26 V, (III) 0.42 V and (IV) comparative EIS of PCz-WO_3/4 at OCP, 0.26V and 0.42V *vs*. Ag/AgCl in 0.5 M H_2SO_4 + 1.0 M HCOOH. The inset of Fig. 8I to 8IV shows a zoomed view of similar and respective EIS plots.

Based on previous works and the above observations, it is concluded that the electro-oxidation of FA over nanocomposite proceeds with the following possible mechanism close to Pt-modified Ta_2O_5 [137]: (a) interaction of formate ions by diffusion-dominated process over or inside the nanocomposite, (b) removal of acidic protons, (c) abstraction of H^+ by electron-rich PCz of PCz-WO_3 nanocomposite as given below:

$$WO_3 + HCOOH \rightarrow WO_3\text{-}(HCOOH)_{ads.} \quad \text{(eq. 3.1)}$$

$$WO_3\text{-}(HCOOH)_{ads.} \rightarrow WO_3\text{-}(HCOO)_{ads.} + H^+ + e^- \quad \text{(eq. 3.2)}$$

$$WO_3\text{-}(HCOO)_{ads.} + PCz \rightarrow PCz\text{-}H + CO_2 \qquad \text{(eq. 3.3)}$$

The present work is compared with earlier published literature, as summarized in table 3.3. We observed that most of the FA oxidations were carried out using CV, LSV, and DPV techniques in the presence of FA mixed with weak supporting electrolytes. At the same time, it can also be exemplified that most of the modification of the electrodes were performed with noble metals in a conducting matrix that allows oxidation in the range from 0.2 to 0.8 V. Our proposed noble metal-free electrode is well suited for the oxidation of FA at relatively lowest potential compare to most of the work.

Table 3.3: Various modified electrodes for the oxidation of formic acid

SN.	Electrode	Electrolyte (in M) (H_2SO_4+ HCOOH)	$V_{anodic\ peak}$ (in V)	Electrochemical techniques	References
1	Pd/C	$0.1^{\#}$ + 2.0	0.40*vs*NHE	CV	[138]
2	PdCo/MWCNTs	0.5 + 0.1	0.28*vs* NHE	CV	[139]
3	Pt/PNI/GCE	0.5 + 0.5	0.35*vs*SCE	CV	[107]
4	Pt/PCZ/GC	0.5 + 0.5	0.40 vsSCE	CV	[54]
5	Pt-Ru/PCZ/GC	0.5+ 0.5	0.47*vs*SCE	CV	[54]
6	PtPb-x-OMCS	0.1 + 0.5	0.37*vs* Ag/AgCl	CV	[140]
7	Pin–SnO_2	0.5 + 1.0	0.34 *vs* Ag/AgCl	DPV	[53]
8	Au-PIn	0.5 + 1.0	0.49 *vs* Ag/AgCl	DPV	[106]
9	Pt/GC	0.1 + 0.5	0.20*vs* SCE	CV	[114]

10	GC/PCZ/Pt	0.1 + 0.5	0.29 *vs* SCE	LSV	[114]
11	Pd_xLa_y/rGO	0.25 + 1.0	0.66 *vs* Ag/AgCl	CV	[141]
12	PdBi	0.5 + 0.5	0.35 *vs* SCE	CV	[142]
13	Pt/PANi/GC	0.5+ 0.3	~0.30*vs* Ag/AgCl	CV	[51]
14	Pt ⎪ PEDOT,PEDOT-nw/NP-Pt	0.1##+ 0.1	0.60 vs SHE	CV	[143]
15	Pd/Nf–CNT	0.5# + 0.5	~0.40	LSV	[144]
16	Pt@PVF-PPy	0.5 + 0.5	0.84 vs. SCE	CV	[145]
17	Pd_xCu_{100-x}/N-rGO	0.5 + 0.5	~0.15 vs SCE	CV	[146]
18	Phen/Pt	0.5# + 1.0	0.45 *vs.* Ag/AgCl	CV	[147]
19	Pt-MnOx/GC	0.0 +0.3	0.30	CV	[101]
20	Pt–M (M = Co, Ni, or Cu) THH NPs	0.5 + 0.5	~0.5 *vs.* RHE	LSV	[148]
21	PCz-WO_3	0.5 + 1.0	0.26 *vs.* Ag/AgCl	DPV	This work

#$HClO_4$and ##KPF_6 electrolytes are used.

3.4. Conclusion

Various PCz-WO_3 nanocomposites were synthesized successfully by the *in-situ* interfacial polymerization method in the presence of different weight ratios of WO_3 and fixed amounts of carbazole monomer. Nano WO_3 is polycrystalline, having an average crystallite size of 42.57 nm existing as diffused cubical-in-shape. On the other hand, PCz has a randomly oriented large flake-type shape with high aspect ratios. These identities are retained even after *in-situ* polymerization. PCz can oxidize FA by direct pathway, while nano WO_3 favors both direct and

indirect pathways. However, in the nanocomposites form, the FA electro-oxidation is dominated by the direct path and oxidation potential shifted to lower potentials (from 0.36 to 0.26 V). Based on the above observations, the nanocomposite PCz-WO_3/4 has a better CO tolerance ability than PCz-WO_3/1 and PCz-WO_3/2 due to optimal synergism between individual components. This phenomenon is stable up to a given period. No doubt, PCz impedes the charge transfer between reference and working electrodes but enhances the abstraction of protons near the vicinity of WO_3 particles by its available electron pairs and hence supports the direct oxidation process. Thus, our proposed noble metal-free electrode is well suited for FA oxidation via the direct pathway at the lowest potential compared to most of the earlier works.